CDF Note 9150

W'-like Resonances in the $t\bar{b}$ Decay Channel with 1.9 fb^{-1}

The CDF Collaboration
URL http://www-cdf.fnal.gov
(Dated: January 3, 2008)

We use the tools of the single top analysis to search for resonant $t\bar{b}$ (+c.c) pair production in a 1.9 fb^{-1} sample of $p\bar{p}$ collisions. For b-tagged events in the W+2 and W+3 jets channels, we look for unexpected structure in the spectrum of M_{WJJ}, the total invariant mass of the reconstructed W boson and two leading jets. Expected contributions from Standard Model (SM) processes are derived from selections and background studies of the single top analysis. Resonant $t\bar{b}$ production is modeled as a simple W' with SM-like couplings to fermions. We establish expected sensitivity over the W' mass range from 300 GeV/c^2 to 950 GeV/c^2, derive 95% CL upper limits for $\sigma \cdot BR(W' \to t\bar{b})$ as a function of the W' mass and compare to expectation.

Preliminary Results for Winter 2008 Conferences

I. INTRODUCTION

The recent progress in single top methods at CDF can be applied to search for unexpected new production mechanisms for $t\bar{b}$ $(+c.c.)$ at large q^2. Resonant tb production is often described in terms of massive W-like bosons, generically called W', that appear in models with left-right symmetry [1], extra dimensions [2], Little Higgs [3], and topcolor [4]. For simplicity, we will refer to our search for a W'-like tb resonance as a search for W'.

We search for events of the form $W' \to tb \to Wbb \to l\nu jj$ (W+jets). Prior W' searches [5] have generally focused on the $W' \to l\nu$ channel, which gives better statistics. The simplest manifestation of a tb resonance would be an unexpected narrow structure in the reconstructed invariant mass of the W and two leading jets (M_{Wjj}) and a Jacobian peak in the transverse momentum of the leading b jet or reconstructed top.

This study is an update of our recent CDF result [6] in 1 fb^{-1} which set limits of $M_{W'} < 760$ GeV/c^2 for the case of $M_{W'} > M_{\nu_R}$ and $M_{W'} < 790$ GeV/c^2 for the case of $M_{W'} < M_{\nu_R}$. Here, using the selection and background techniques of the single top analysis, we search for resonant tb states in 1.9 fb^{-1} of $p\bar{p}$ collisions at $\sqrt{s} = 1.96$ TeV. Modeling the resonance as a simple W'-like boson, we set limits on the production cross-section as a function of the pole mass and effective gauge coupling.

II. DATA SAMPLE AND EVENT SELECTION

A. Data Sample

We use 1.9 fb^{-1} of CDF Run II data taken through May 13, 2007. The CDF detector is described in detail in [8]. We employ the same W+jets event selection as the Single-Top group for their 1.9 fb^{-1} result [7], also including a variety of new muon types.

We require exactly one lepton with large transverse momentum ($P_T \geq 20$ GeV) and isolation from jets, large missing transverse energy ($\not\!\!E_T \geq 25$ GeV), two or three energetic jets ($E_t \geq 15$ GeV and $|\eta_{detector}| < 2.8$), and at least one of the jets must have a displaced secondary vertex (b-tag).

In the data we find 1476 candidate events with 2 jets and 653 events with 3 jets, consistent with the single top analysis.

B. Event Reconstruction

In order to reconstruct the total mass of the tb system, we must reconstruct the longitudinal component of the neutrino momentum: $\nu\ P_z$. If we assume the mass of the W to be 80.448 GeV/c^2, we can solve the resulting quadratic equation for $\nu\ P_z$. In the case of complex solutions (when the transverse mass sums to more than the mass constraint), we assign $\nu\ P_z$ to the real part.

With the neutrino four-momentum now fully specified, we can reconstruct the mass of the W and two leading jets: M_{Wjj}. In addition, we construct a variety of other kinematic variables which will be used to validate our model.

III. BACKGROUND MODEL

We use the same background normalizations and shapes as the single top analysis. Table I summarizes our background (BG) components and their predicted normalization in each channel.

The tagged BG templates all come from weighting pretag events. The weights correspond to each event's single or double tag probability from the mistag matrix, including corrections for asymmetry. Samples are also weighted according to their luminosity. We will briefly discuss the construction of the major background components.

A. W+Heavy Flavor ($Wb\bar{b}, Wc\bar{c}, Wcj$)

Because our method for heavy flavor prediction is known to underestimate the heavy flavor contribution, a MC correction factor is applied. This correction factor is obtained by constructing templates for W+bottom, W+charm, and W+light flavor and fitting them to data the 1 jet control region. Fixing the light flavor contribution to expectation, we measure a correction factor of 1.4 ± 0.4 for both bottom and charm. This scaling leads to good agreement with data across all jet multiplicities.

Background	2 Jet 1 Tag	3 Jet 1 Tag	2 Jet 2 Tags	3 Jet 2 Tags
$Wb\bar{b}$	361.2 ± 108.8	107.8 ± 32.5	48.2 ± 15	17.8 ± 5.5
$Wc\bar{c}$	406.9 ± 125.5	106.5 ± 32.7	5.5 ± 1.8	2.9 ± 0.9
Mistagged LF	275.4 ± 34.8	81.6 ± 10.5	1.2 ± 0.3	0.8 ± 0.2
Non-W	52.4 ± 21	18.4 ± 7.3	1.2 ± 0.5	0.2 ± 0.1
$t\bar{t}$ (dilepton)	33.9 ± 4.7	27.5 ± 3.8	9.4 ± 1.5	9.3 ± 1.5
$t\bar{t}$ (lepton+jets)	69.3 ± 9.7	197.4 ± 27.5	13.9 ± 2.3	57.6 ± 9.5
Single Top (t-channel)	27.3 ± 3.8	8.7 ± 1.2	8 ± 1.3	2.8 ± 0.5
Single Top (s-channel)	51.9 ± 7.6	13.6 ± 1.9	1.5 ± 0.3	2.2 ± 0.4
WW	36.1 ± 4	12.8 ± 1.4	0.2 ± 0	0.3 ± 0
WZ	14.7 ± 1.1	4.2 ± 0.3	2.9 ± 0.3	0.9 ± 0.1
ZZ	0.5 ± 0	0.2 ± 0	0.1 ± 0	0 ± 0
Z+Jets	21.5 ± 3.2	8.7 ± 1.3	1 ± 0.2	0.6 ± 0.1
Total Prediction	1351.1 ± 238.1	587.5 ± 73.0	93.0 ± 17.4	95.5 ± 12.6
Data	1273	520	89	97

TABLE I: Background Predictions - CDF Run II Preliminary: 1.9 fb^{-1}

To construct the W+bottom and W+charm templates, all the heavy and light flavor samples are combined together, and events are assigned to templates based on the generator-level flavor of the jets. Thus some bottom events come from W+charm samples and vice versa.

B. Mistags

The mistag shape is modeled using with Monte Carlo. As with heavy flavor, the light flavor templates are constructed by combining all heavy and light samples and selecting events based on their generator-level flavor. Thus some mistag events come from heavy flavor samples and not simply $W + 2p$ and $W + 3p$. Again, all backgrounds use properly weighted pretag events.

C. Non-W

The non-W shape is constructed beginning with anti-electrons: the electrons-like events which fail two of the five standard non-kinematic ID cuts. These are treated as tight electrons, and should provide a good kinematic description of the non-W background. For high-η electrons, we model their non-W shape with a sample of jets with high track multiplicity and high electromagnetic to hadronic energy fraction.

We do not have sufficient statistics to require b-tags and thus we use tag-probability weighted pretag events, analogous to what is done for mistags.

Finally, the normalization of the non-W shape is determined by fitting the $\not\!\!E_T$ distribution in the tagged data.

D. Background Templates

We collect backgrounds with similar kinematics into a common histogram (template). We have five templates in total: W+bottom, W+charm, mistag/non-W, $t\bar{t}$, and single-top. Table II shows the composition of each of the templates and Figure 1 shows their shapes.

Template	BG Components
W+bottom	$Wb\bar{b}$, WZ, Z+Jets
W+charm	$Wc\bar{c}$, Wc, WW
$t\bar{t}$	$t\bar{t}$ (dilepton), $t\bar{t}$ (lepton+jet)
mistag/non-W	Mistagged LF and Non-W
single top	Single Top (s-channel), Single Top (t-channel)

TABLE II: Composition of Background Templates

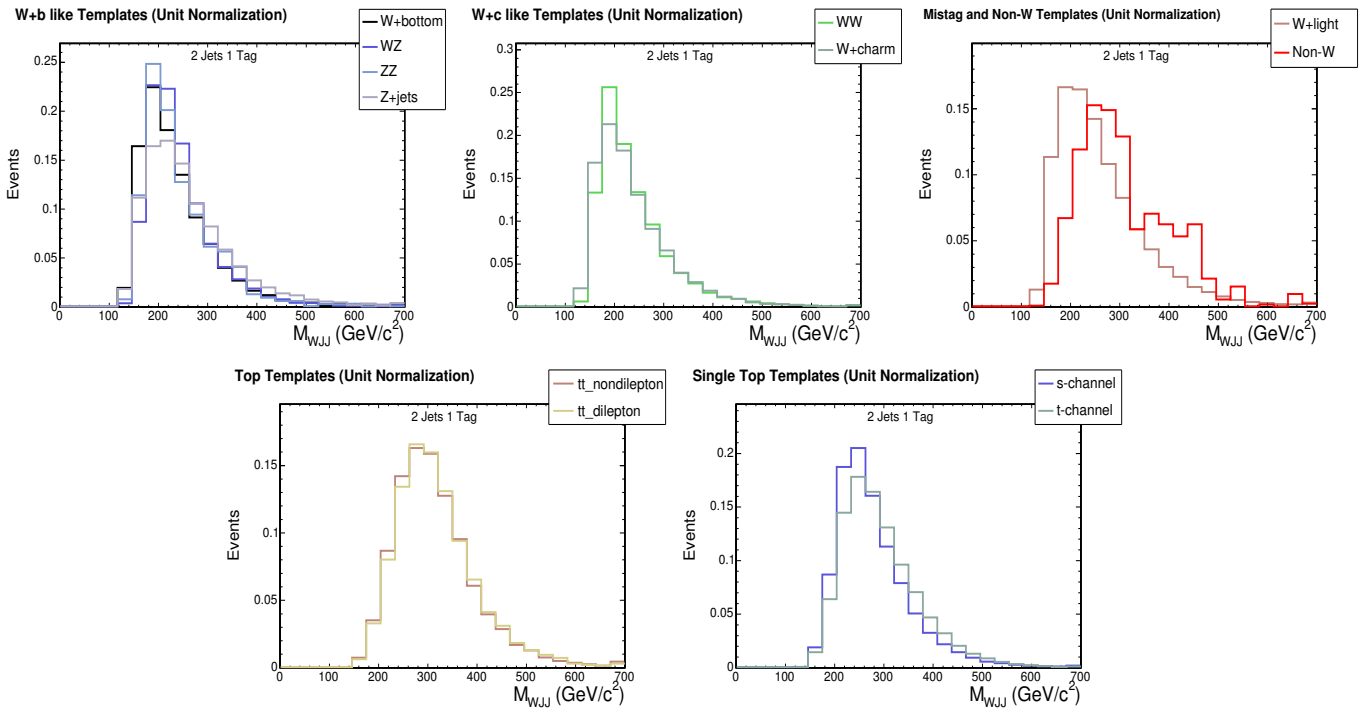

FIG. 1: The BG component shapes (normalized to unit area) of the five template groupings.

E. Background Validation

We compare our full background model to the data in over 40 different control distributions, separately for one, two, and three jets, separated by tag multiplicity. Because we initially considered also using the anti-tag distribution, we have plots for them as well. Our models are in agreement with the data in the control regions, and our distributions are consistent with prior validation for single top. Figure 13 shows the lepton P_T distribution, Figure 14 shows the energy of the lead jet, Figure 15 shows the $\not\!\!E_T$ distribution, and Figure 16 show the transverse W mass. All are in good agreement with expectation.

IV. W' SIGNAL

A. R and L-Handed W' Models

The Lagrangian describing the W' coupling to fermions can be written as [9]:

$$\mathcal{L} = g\bar{f}_i\gamma_\mu(C^R_{ij}P_R + C^L_{ij}P_L)W'f_j \tag{1}$$

where $P_{L,R} = (1 \pm \gamma_5)/2$ are the projection operators, g is the gauge coupling, and the $C^{L,R}_{ij}$ are arbitrary coupling that differ for quarks and leptons. We assume that the W' has purely right-handed or left-handed couplings. Figure 2 shows the dominant s-channel diagram for W' production. Contributions from the $t-$ and $u-$ channels are suppressed by the large W' mass.

There are two differences between the R-handed and the L-handed W' models:

- ⋆ The L-handed W' bosons are expected to interfere with the standard model $W \to t\bar{b}$ process, also known as $s-$channel single-top production. A discussion of this interference is given later in the text. The R-handed W' bosons do not interfere with the $s-$channel single-top due to the different final states.
- ⋆ In regard to R-handed W' models only, we distinguish two cases depending on the mass of the R-handed neutrinos:

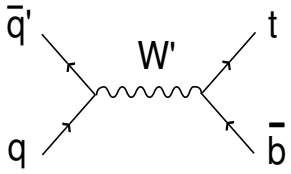

FIG. 2: Representative Feynman diagram for W' production.

a. If $M_{\nu_R} > M_{W'}$ then the R-handed and L-handed $W' \to t\bar{b}$ processes have the same cross-section (modulo the interference point mentioned above)

b. If $M_{\nu_R} < M_{W'}$ then the R-handed and L-handed $W' \to t\bar{b}$ processes have different cross-sections, as the R-handed W' has more decay channels open. This will lead to a lower $W'_R \to t\bar{b}$ cross-section than that of $W'_L \to t\bar{b}$.

In Ref. [9], the W'_L width and cross-sections are calculated neglecting the effect of the Standard Model $W \to t\bar{b}$ process. Following the lead of Ref. [9], we also neglect the interference between the L-handed W' and the $s-$channel single-top. For clarity, we remind the reader that both of these processes are included in the search, W' as signal, and s-channel single-top as part of the background. It is the interference term that is not included, which is a good approximation especially for the high-mass region: $M_{W'_L} \gg M_W$. The effect of interference would be to slightly alter the high tail of s-channel single-top and the low tail of the W'_L process.

If the W/W' interference is neglected, then as far as our analysis results are concerned the W'_L models are identical with the W'_R models if $M_{\nu_R} > M_{W'}$. The Monte Carlo program we used to model both W'_L and W'_R was `PYTHIA` $p\bar{p} \to W' \to t\bar{b}$, where handedness is irrelevant since no W/W' interference is assumed. The only separation of models appears for the R-handed W' bosons if we do or do not allow extra decays to R-handed leptons − cases `a.` and `b.` above − and comes in only through the different $W'_R \to t\bar{b}$ branching fraction. In other words, all distributions are the same, but the `a.` and `b.` normalizations are different.

The theoretical prediction for these two cases is shown is Table III.

W' Mass (GeV/c^2)	$\sigma \cdot BR(tb)$ (pb) $M_{W'} < M_{\nu_R}$	$\sigma \cdot BR(tb)$ (pb) $M_{W'} > M_{\nu_R}$	Exp Events $M_{W'} < M_{\nu_R}$	Exp Events $M_{W'} > M_{\nu_R}$
500	7.95	5.92	531	396
600	2.79	2.1	173	130
700	0.974	0.743	57	43.5
800	0.337	0.262	18.4	14.3
900	0.116	0.0932	6.08	4.88

TABLE III: Expected W' Signal - CDF Run II Preliminary: 1.9 fb^{-1}

B. W' Monte Carlo Generation

We model resonant $t\bar{b}$ production with a heavy, charged boson (W') with the same fermion couplings as the W.We assume a model without interference with the SM W boson and associated single top production. It has been shown that this is valid approximation below 900 GeV/c^2. Our W' is thus a general model of any new state appearing as, or approximated by, a Lorentzian enhancement in a narrow region of the $M_{t\bar{b}}$ spectrum.

We generated Monte Carlo (MC) samples for W' masses from 300 GeV/$c^2$to 950 GeV/c^2 in 50 GeV/c^2 increments for large masses. The W' is constrained to decay via $t\bar{b}$, and we further require that the top decay leptonicly ($W \to l\nu_l$ for $l = e, \mu,$ *or* τ).

Top-quark polarization impacts angular event variables but has a negligible effect on kinematic variables like $M_{t\bar{b}}$, H_t, etc. Our W' search does not depend on the detailed modeling of top-polarization effects.

C. W' Kinematics

W' decay follows the two-body decay formula, which states that the energy of the b-quark in the W' rest frame is:

$$E_b = \frac{M_{W'}^2 + M_b^2 - M_t^2}{2M_{W'}}. \quad (2)$$

Because a massive W' is produced nearly at rest, the W' rest frame is approximately the lab rest frame. Thus we expect to observe a very energetic b-jet, with nearly half the energy of the W' mass. See the systematics section for discussion of the effect on the b-tag MC scale factor. MC studies show that this jet is the lead jet for 91% of events. The top quark is also produced with a significant boost.

Due to the energetic nature of the W' decay, we may expect to see enhanced signal separation in the lead jet E_T distribution and H_T in addition to the total mass. Pseudo-experiments have shown that M_{WJJ} is still the distribution we expect to be the most sensitive, and will be our variable of merit. A comparison of the signal and background shapes can be seen in Figure 3.

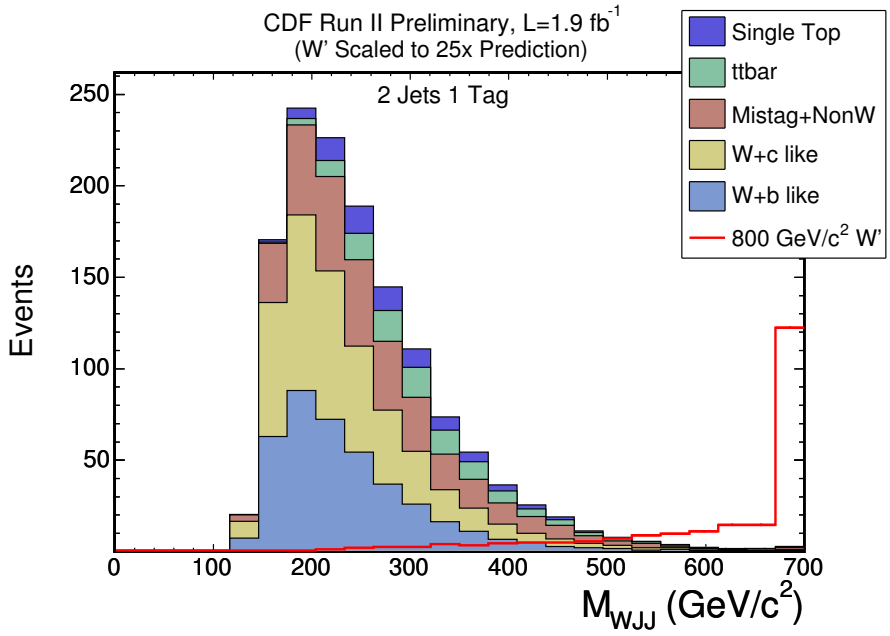

FIG. 3: Comparison of signal and BG shapes for $M_{W'}$ in the dominant 2 jet 1 tag channel. The W' signal of 800 GeV/$c^2$is normalized 25 times larger than predicted by theory.

V. CALCULATION OF EXPECTED LIMITS IN M_{WJJ}

We search for evidence of W' production in M_{WJJ} by performing ensembles of pseudo experiments (PE's) in which we compare the agreement of two hypotheses with Poisson-fluctuated data (pseudo data).

The null hypothesis, H_B, asserts that the pseudo data are fully described by the standard model as characterized by our background model. The signal + background hypothesis, H_{S+B}, asserts that the pseudo data data are comprised of the SM background plus some fraction W' events. We define a test statistic to quantify the agreement between the pseudo-data and our hypotheses for a specified signal fraction.

A. Frequentist Test Statistic

We set modified frequentist limits by measuring the agreement of the hypotheses with the data using the ratio of their likelihood values,

$$Q = \frac{\chi^2(data|H_{S+B})}{\chi^2(data|H_B)}, \quad (3)$$

where the χ^2 function is based likelihood. Taking the logarithm, we can define $\Delta\chi^2$.

$$-2\ln Q = \chi^2(data|H_{S+B}) - \chi^2(data|H_B) \equiv \Delta\chi^2 \tag{4}$$

Our variable of merit combines the probability of each of the two hypotheses and is defined by

$$CL_S = \frac{P_S(\Delta\chi^2 \geq \Delta\chi^2_{obsv})}{P_{S+B}(\Delta\chi^2 \geq \Delta\chi^2_{obsv})} \tag{5}$$

B. Calculating Upper Limit

We represent rate and shape uncertainties by assigning a corresponding "nuisance parameter" whose value varies from PE to PE and is drawn from a Gaussian distribution with mean X and standard deviation Y. The mean is specified by the nominal value of the systematic uncertainty, and the width is set by its uncertainty. Thus all systematic uncertainties are modeled internally and their effect is automatically incorporated into the final result.

We construct ensembles of ∼25k PE's and vary the signal fraction in the H_{S+B} hypothesis. Our expected limits are determined by finding the amount of signal needed in order for 95% of the H_{S+B} Q-values to be larger than the median Q for H_B. We can similarly calculate the $\pm1\sigma$ deviations from the expected limit by finding the amount of signal needed for 95% of the H_{S+B} Q-values to be larger than the $\pm1\sigma$ Q for H_B. The observed limit is set when 95% of the Q-values larger than Q for the data come from H_{S+B}, i.e. $CL_S \leq 0.05$.

C. Checking Results

We first verifyied that our expected limit is consistent with scaling our 1 fb^{-1} result by square root of the increase in luminosity. We also verified that our fit technique gives a linear response across a range of input signal levels. Figure 5 shows our result. We also looked at whether our expected limits appear consistent between electrons and muons. This is shown in Figure 4. From this plot we can also conclude that adding non-trigger muons does add significantly to our sensitivity. This is because using a large $\not\!\!E_T$trigger for those events makes them more like an energetic signal with large $\not\!\!E_T$.

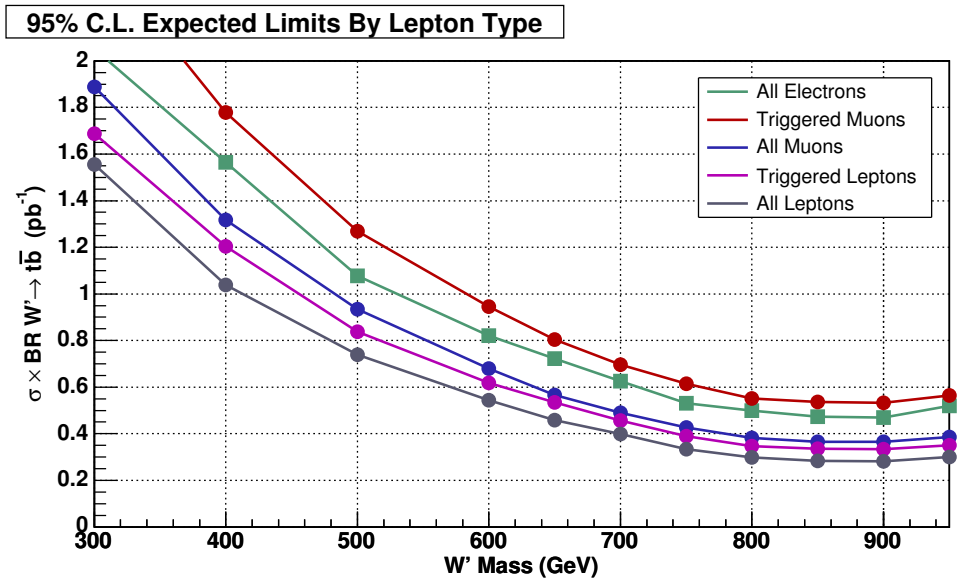

FIG. 4: Comparison of expected limits among various lepton types.

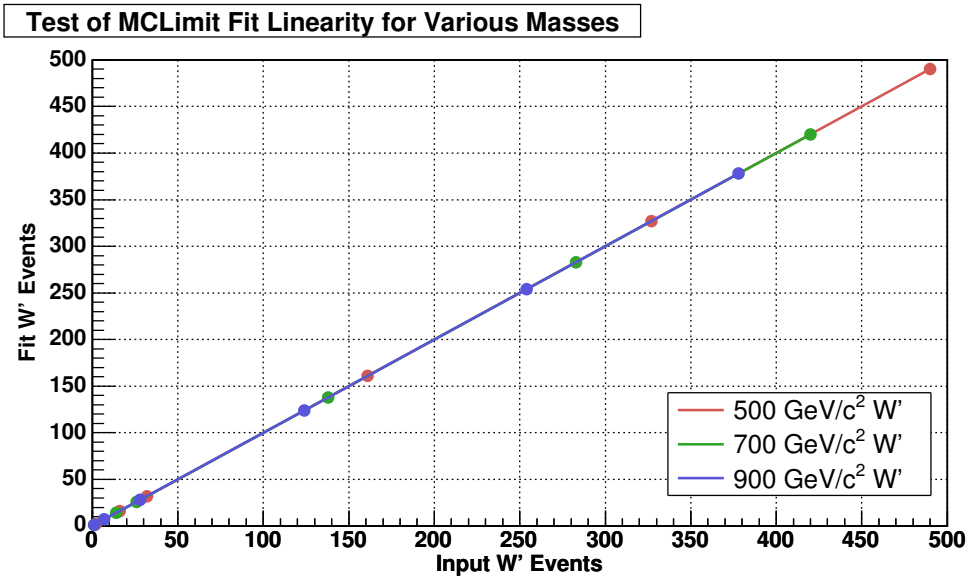

FIG. 5: Check of `Minuit` fit results for various signal inputs.

D. Combining Channels

The M_{WJJ} distribution in the four channels (2 jets 1 tag, 3 jets 1 tag, 2 jets 2 tags, and 3 jets 2 tags) can be combined for enhanced signal sensitivity. This procedure calculates the total test statistic by using the same nuisance parameters for all four channels and summing the χ^2 across the bins in all channels: $\Delta\chi^2_{total} = \Delta\chi^2_{2J1T} + \Delta\chi^2_{3J1T} + \Delta\chi^2_{2J2T} + \Delta\chi^2_{3J2T}$.

Figure 6 compares the expected limits in each channel. Most of the sensitivity comes from the 2 jets 1 tag channel. There is little top contamination in this channel. The 3 jet channels have more top BG, so that the signal shape is only well seperated from BG at the highest masses.

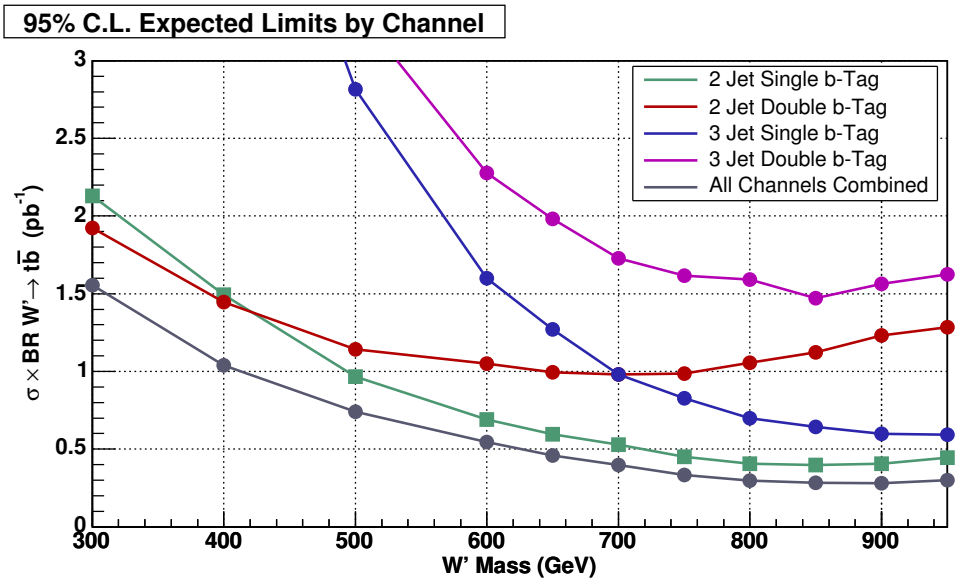

FIG. 6: Expected limits for each channel individually. The 2 jet 1 tag channel, with its small top fraction, is the most sensitive.

VI. SYSTEMATIC UNCERTAINITES

Our full systematic uncertainty includes contributions from jet energy scale (JES), the b-tag scale-factor, initial state radiation (ISR), final state radiation (FSR), the ALPGEN Monte Carlo Factorization/Renormalization (Q^2) scale, mistag shape, non-W shape, parton distribution functions (PDF), luminosity, and lepton identification. The effect of including systematic errors on our limits can be seen in Figure 7. The b-tag scale factor uncertainty is our second largest source of uncertainty, and requires special treatment. First, we discuss the treatment of rate and shape systematic uncertainties in our pseudo experiments. Then we discuss our method for estimating each systematic uncertainty.

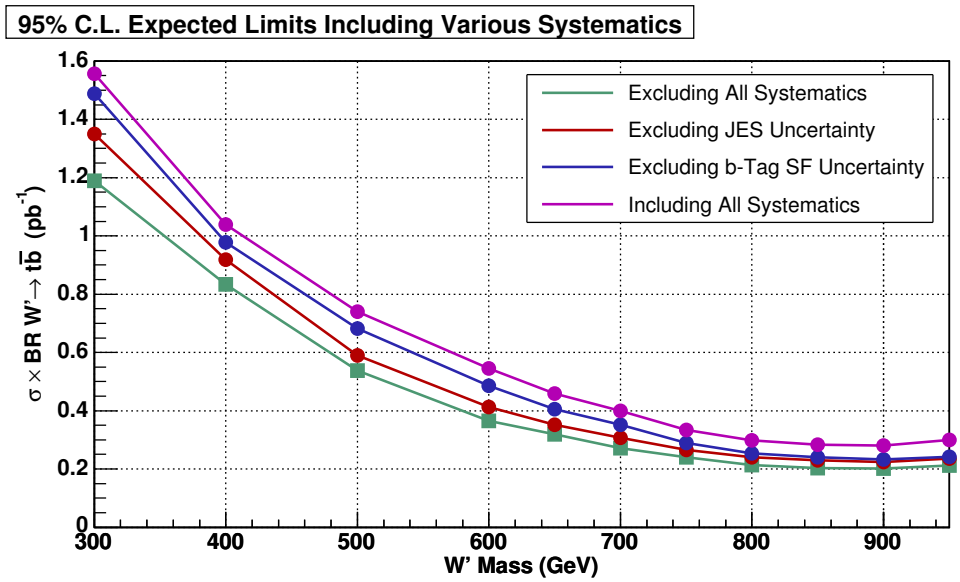

FIG. 7: Expected limits included various systematic uncertainties. The JES and b-tag scale factor uncertainties are the most significant uncertainties. with all systematics applied.

A. Systematic Uncertainties in Pseudo Experiments

We incorporate normalization uncertainties by assigning a corresponding nuisance parameter in our PE's. These parameters are independently varied within a Gaussian constraint during each PE. Thus the mean of the Gaussian fluctuation for a particular nuisance parameter is the nominal expected normalization, and the width is set by the uncertainty on that normalization.

Shape uncertainties are also treated by assigning them a nuisance parameter which can vary within a Gaussian constraint. The value of the nuisance parameter for a particular PE corresponds to the amount by which we shift our template for that PE. This is often referred to as template morphing. All template morphing is performed using a horizonal interpolation algorithm.

To generate each shifted template, our PE code uses the unshifted original shape and the $\pm N\sigma$ (N may differ for various systematic uncertainties) shifted shapes to interpolate any amount of shape variation within the bounds of $\pm N\sigma$. Because extrapolation beyond this range is less certain, we truncate the nuisance parameter for the shape variation at $\pm N\sigma$. Thus $\pm$ templates input into the code set the bounds in which we can vary the template morphing.

We include all shape variations simultaneously in our expected limit calculations. The program calculates the shape variation for each parameter independently during a PE, then averages all the shifted templates for the overall shift. We acknowledge that this procedure neglects the correlations (or anti-correlations) between sources of systematic uncertainty. We anticipate the overall impact of correlations is small among our major systematic uncertainties and we do not attempt a more sophisticated treatment at this time.

B. Estimation of Each Systematic Uncertainty

Jet Energy Scale (JES): This is our dominant systematic. We generate the $\pm 1\sigma$ JES shifted shapes for our signal and MC backgrounds by adding all sources of jet uncertainty in quadrature. We use extrapolate the $\pm 1\sigma$ shapes shifts (including normalization changes) out to $\pm 3\sigma$. We use the 3σ varied templates to vary the JES within these bounds during the PE's.

B-tag scale factor: As shown in Figure 7, the b-tag scale factor uncertainty is second largest source of systematic uncertainty, This factor corrects the b-tagging rate in MC to match the data, and is currently measured with a sample without statistics for measurement beyond 120 GeV. Though the BG uncertainty can be treated in the normal fashion (4% rate uncertainty), a massive W' can produce jets well above 300 GeV, and thus we must attempt to quantify the uncertainty for values far larger than for which it is measured.

Our treatment is to use lead jet E_T dependent functions based on extrapolation from the well-measured region. We use these function as weights to produce shifted templates for the b-tag uncertainty. The effect on shape is rather small, even at high W' mass. The effect on rate is very large, ranging from 14% at low mass to 40% at high mass. This approach is quite conservative, and the error should be reduced by adding more data to the scale factor measurement, or switching to a better populated control sample.

Initial/Final State Radiation (ISR/FSR): We generated more or less ISR and FSR shifted samples, and assume the more sample is a $+1\sigma$ shift and the less is a -1σ shift. Thus we vary ISR/FSR within this range during our PE's.

ALPGEN Factorization/Renormalization scale (Q^2): W+jets MC is produced using `ALPGEN`. The choice of factorization/renormalization scale (Q^2) impacts the shape of those W+jets MC samples. To estimate the uncertainty arising from the Q^2 scale, we created alternate shape templates for $Wb\bar{b}$ using $Q^2 = 2$ and $Q^2 = 0.5$. We consider only the variations in shape. We include these alternate shape templates as 1σ variations in our pseudo experiments. Although the W+charm and W+light flavor templates are also affected by Q^2, we assume the effect for charm is small and that the mistag shape uncertainty (discussed below) subsumes any Q^2 dependence.

Mistag Model: We estimate the uncertainty in using W+2p and W+3p pretag MC to model the mistag shape by treating an alternative template made from pretag data as a 1σ shape variation when performing our PE's.

Non-W Model: Due to the small non-W fraction remaining after our QCD cuts, we do not expect to be sensitive to changes in the non-W shape. Nonetheless, we estimate our shape uncertainty by substituting the jet-electron sample for the anti-electron sample, and using this as a 1σ shape variation when performing our PE's.

Parton Distribution Function (PDF):: In 1 fb^{-1} we estimated the impact of using different parton distribution functions using event reweighting. The largest shift was 4%, which we subsequently use as our PDF uncertainty for the full signal range.

Luminosity, Lepton ID: The signal and BG acceptances include rate uncertainty from several sources. Lepton ID is a rate uncertainty which varies with lepton type. It's largest for the non-trigger muons ($\sim$2%). Dataset luminosity for our sample is uncertain to within 6%. Generally treat small rate uncertainties as uncorrelated and add them quadrature. Since including correlations gives a smaller total, our approach is conservative and easily negligable compared to JES and b-tag scale factor uncertainty.

VII. FINAL RESULTS

A. Limits on W' Mass

Figures 8 and 9 show the signal distribution in each of the four channels.

Figures 10 and 11 show our final result. We set an asympotic high mass limit of 0.27 pb at 95% confidence level. The observed limit is plotted with the theoretical prediction [9], allowing us to set a lower limit on the W' mass of such a model. We set a limit with 95% confidence of $M_{W'} < 800$ GeV/c^2 for the case $M_{W'} > M_{\nu_R}$ and a limit of $M_{W'} < 825$ GeV/c^2 for the case $M_{W'} < M_{\nu_R}$.

Compared to our result in 1 fb^{-1}, the observed limit is in much better agreement with expectation and no significant

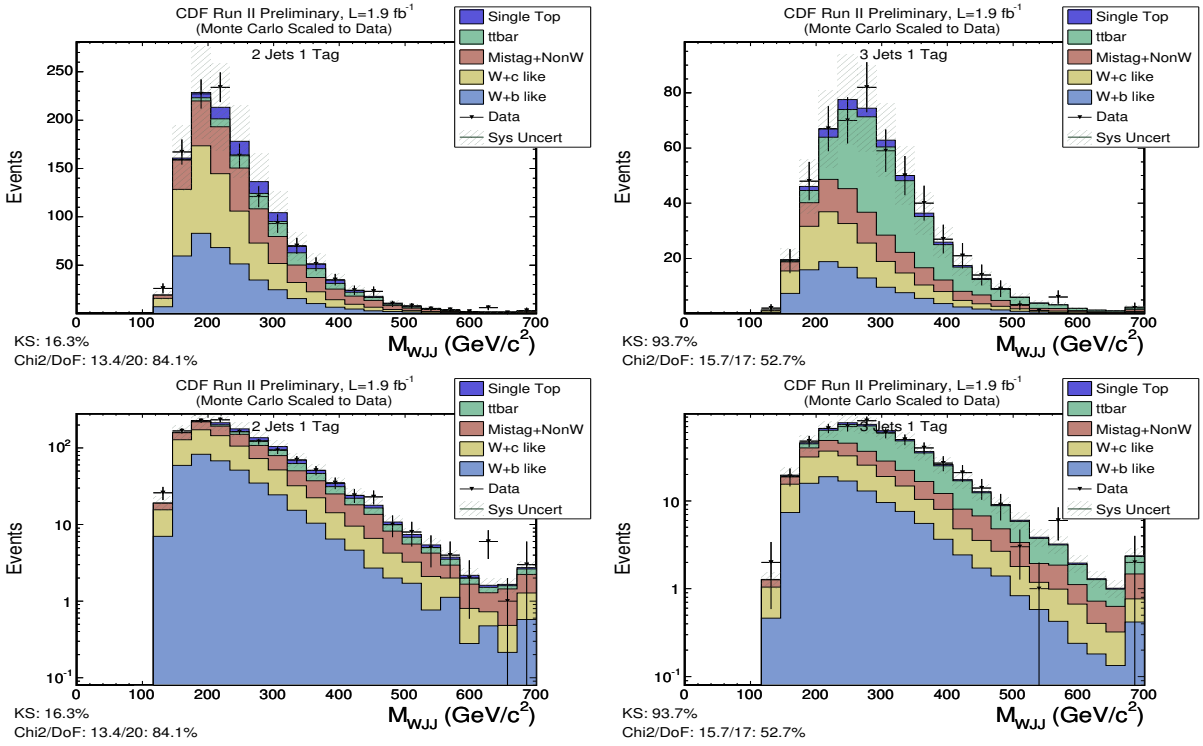

FIG. 8: Comparison of the M_{WJJ} model to the data for the 2 jets 1 tag channel (left) and the 3 jets 1 tag channel (right). The bottom row shows the plots on a log scale.

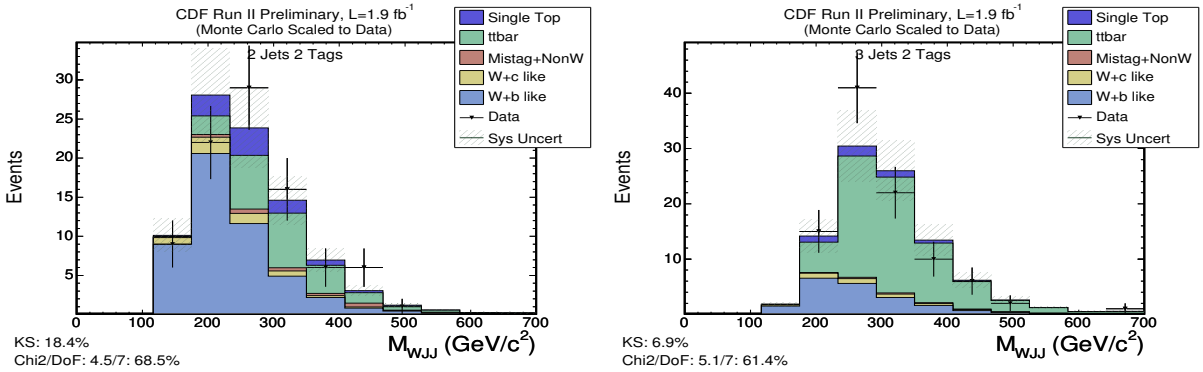

FIG. 9: Comparison of the M_{WJJ} model to the data for the 2 jets 2 tags channel (left) and the 3 jets 2 tags channel (right).

excess is observed over the full range.

B. Limits on W' Coupling Stregth

The last part of our discussion regards setting limits in the $M_{W'} - g$ plane. As seen in the beginning of this section, the gauge coupling $g_{R,L}$ comes in as a multiplicative parameter in the Lagrangian. Given that there are two $qW'q$ vertices in the leading order diagram of Fig. 2, the total $p\bar{p} \to W' \to t\bar{b}$ cross-section will be proportional to g^4, where g denotes either the g_R or the g_L coupling depending on the model we are testing. So far we have assumed $g = g_{SM}$. However, this does not have to be the case, and we can test models with different values of g. In fact, if we assume that the width of the reconstructed W' mass distribution is dominated by detector effects then a model with $g \neq g_{SM}$ would have an identical reconstructed W' mass distribution as a $g = g_{SM}$ model, but a normalization which differs

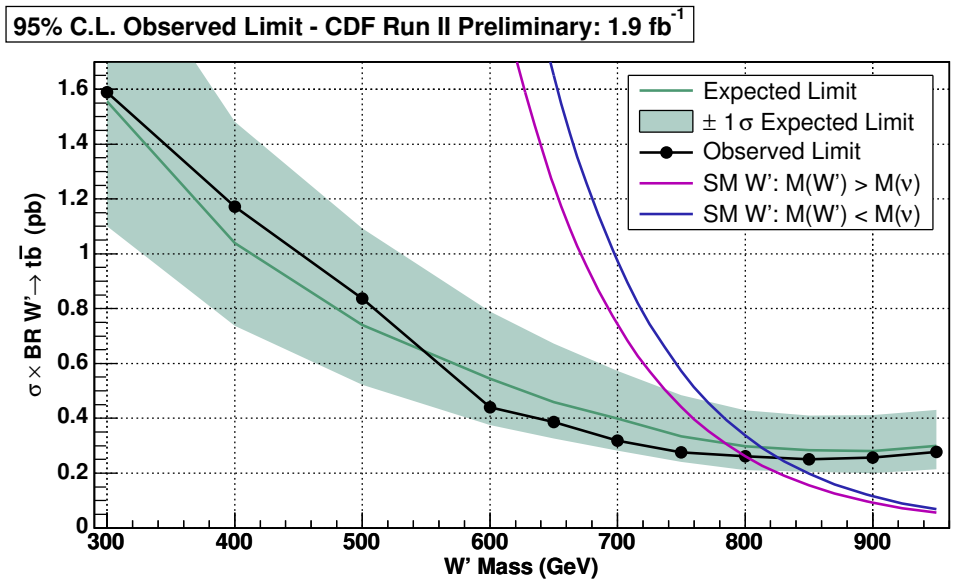

FIG. 10: Observed limit on the W' mass.

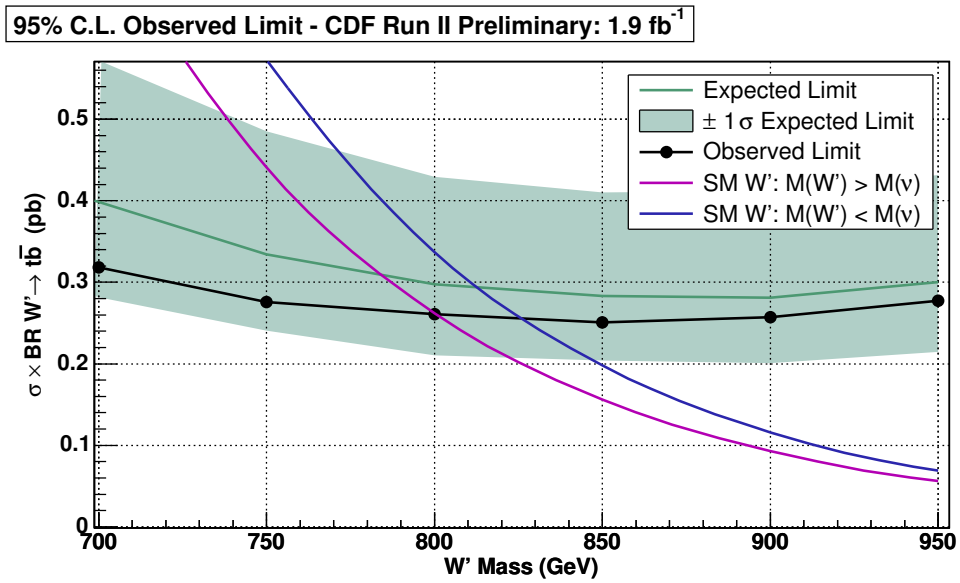

FIG. 11: Observed limit on the W' mass enlarged to show the high mass region.

by a factor of g^4/g_{SM}^4. For a given mass $M_{W'}$ we can adjust g until the cross-section of the model calculated via scaling by g^4/g_{SM}^4 equals the experimentally excluded cross-section. This is precisely how the $M_{W'} - g$ graph shown in Figure 12 is constructed. As seen in this plot, we exclude gauge couplings down to 0.4 g_{SM} for low W' masses and $M_{W'} < M(\nu)$.

VIII. CONCLUSION

We use 1.9 pb^{-1} of CDF Run II data and find no evidence for resonant W' production. We set an asympotic high mass limit of 0.27 pb at 95% confidence level. For a W' with SM couplings which decays via $W' \to t\bar{b}$, we set limits of $M_{W'} < 800$ GeV/c^2 when $M_{W'} > M_{\nu_R}$ and $M_{W'} < 825$ GeV/c^2 when $M_{W'} < M_{\nu_R}$. Constraints on the coupling

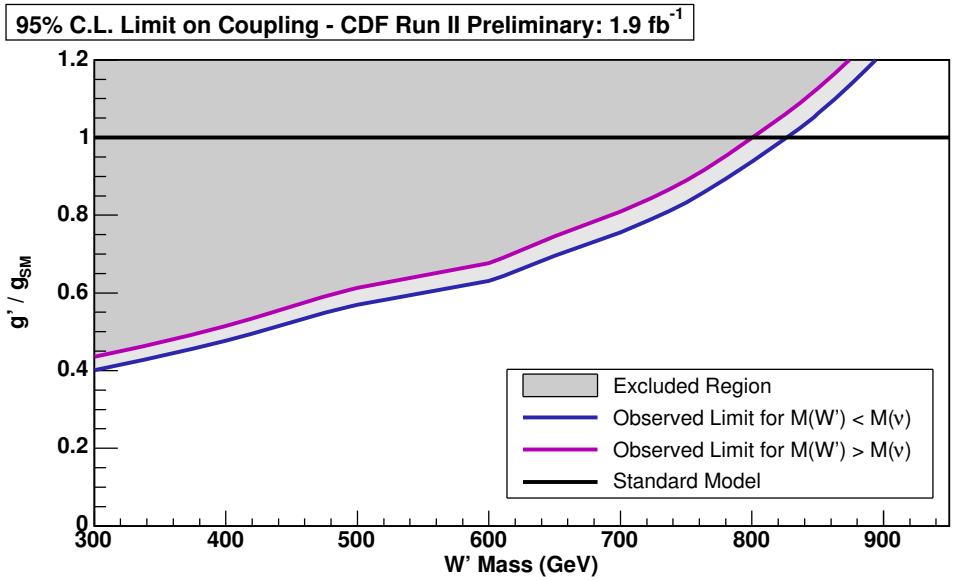

FIG. 12: Observed limits on the ratio of coupling constants, g'/g. The shaded region is exclued.

to fermions are shown in Fig. 12.

[1] J.C. Pati, A. Salam, Phys. Rev.**D10**, 275 (1974)
R. Mohapatra and J. Pati, Phys. Rev.**D11**, 566 (1975).
[2] Y. Mimura, S. Nandi, Phys. Lett. **B538**, 406 (2002)
G. Burdman, B. Dobrescu, E. Ponton, Phys. Rev.**D74**, 075008 (2006).
[3] M. Perelstein, Prog. Part. Nucl. Phys.**58**, (2007). hep-ph/0512128
[4] E. Malkawi, T. Tait, C.P. Yuan, Phys. Lett. **B385**, 304 (1996)
H. Georgi, E. Jenkins, E. Simmons, Nucl. Phys **B331**, 541 (1990).
[5] $W' \to \ell\nu_\ell$ at CDF: The CDF Collaboration, Phys. Rev. Lett. **67**, 2609 (1991).
The CDF Collaboration, Phys. Rev. Lett. **74**, 2900 (1995).
The CDF Collaboration, Phys. Rev. Lett. **84**, 5716 (2000).
The CDF Collaboration, Phys. Rev. **D75**, 091101 (2007).
$W' \to t\bar{b}$ at CDF:
The CDF Collaboration, Phys. Rev. Lett. **90**, 081802 (2003).
$W' \to \ell\nu_\ell$ at DØ:
The DØ Collaboration, Phys. Rev. Lett. **76**, 3271 (1996).
The DØ Collaboration, Phys. Lett. **B358**, 405 (1995).
$W' \to t\bar{b}$ at DØ:
The DØ Collaboration, Phys. Lett. B **641**, 423 (2006).
[6] The CDF Collaboration, Public Note CDF/PHYS/TOP/PUBLIC/8747
[7] The CDF Collaboration, Public Note CDF/PUB/TOP/PUBLIC/8968
[8] F. Abe, et al., Nucl. Instrum. Methods Phys. Res. A **271**, 387 (1988); D. Amidei, et al., Nucl. Instum. Methods Phys. Res. A **350**, 73 (1994); F. Abe, et al., Phys. Rev. D **52**, 4784 (1995); P. Azzi, et al., Nucl. Instrum. Methods Phys. Res. A **360**, 137 (1995); The CDFII Detector Technical Design Report, Fermilab-Pub-96/390-E
[9] Z. Sullivan, *Fully differential W' production and decay at next-to-leading order in QCD*, Phys. Rev. **D66** 075011, (2002). hep-ph/0207290

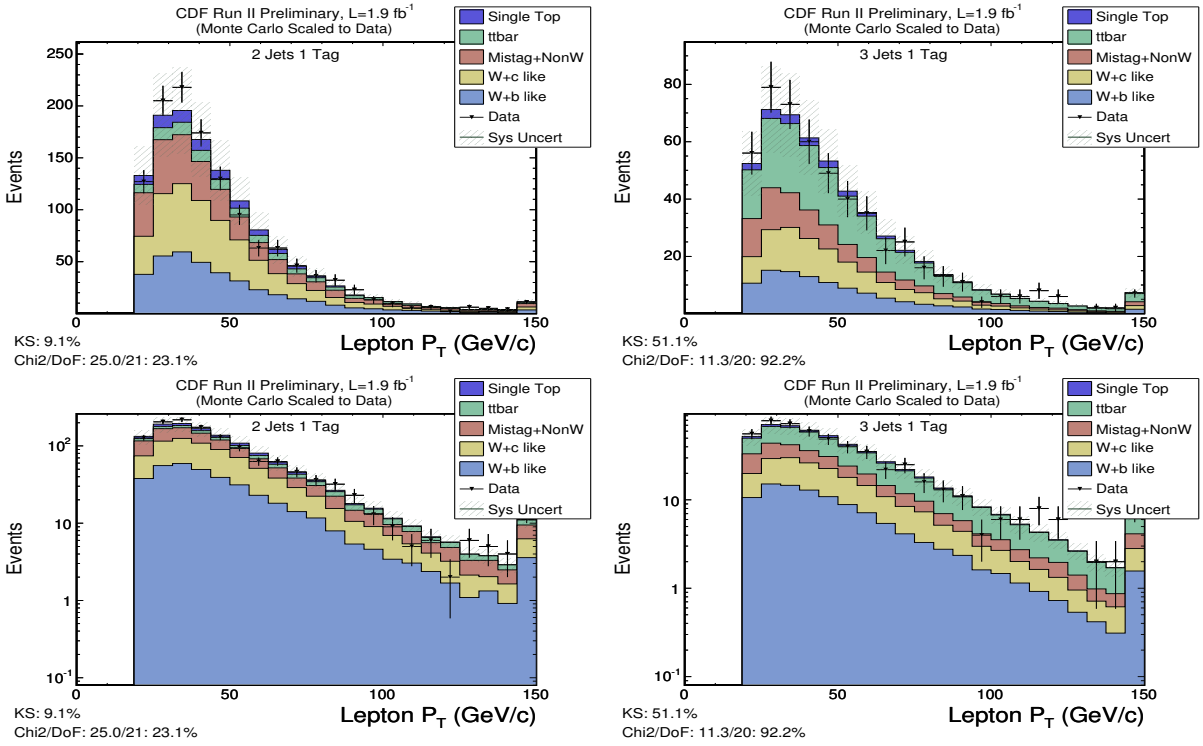

FIG. 13: Comparison of the lepton P_T model to the data for the 2 jets 1 tag channel (left) and the 3 jets 1 tag channel (right). The bottom row shows the plots on a log scale.

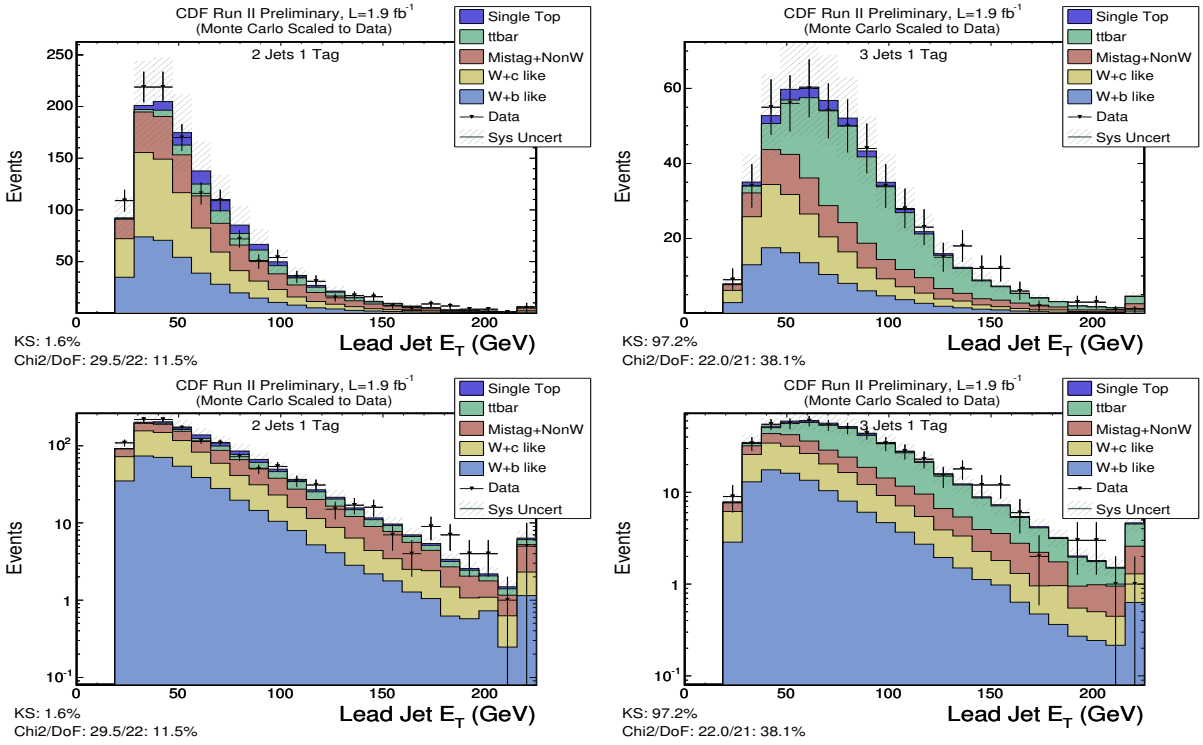

FIG. 14: Comparison of the lead jet E_T model to the data for the 2 jets 1 tag channel (left) and the 3 jets 1 tag channel (right). The bottom row shows the plots on a log scale.

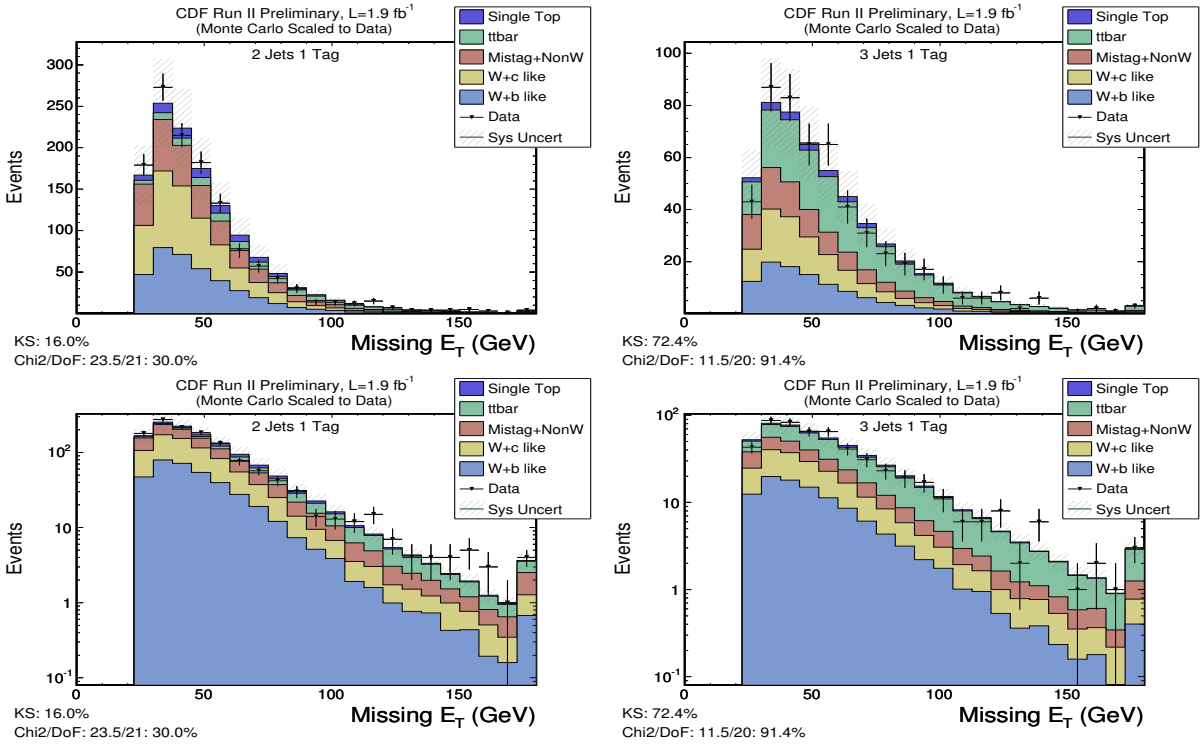

FIG. 15: Comparison of the $\not\!\!E_T$ model to the data for the 2 jets 1 tag channel (left) and the 3 jets 1 tag channel (right). The bottom row shows the plots on a log scale.

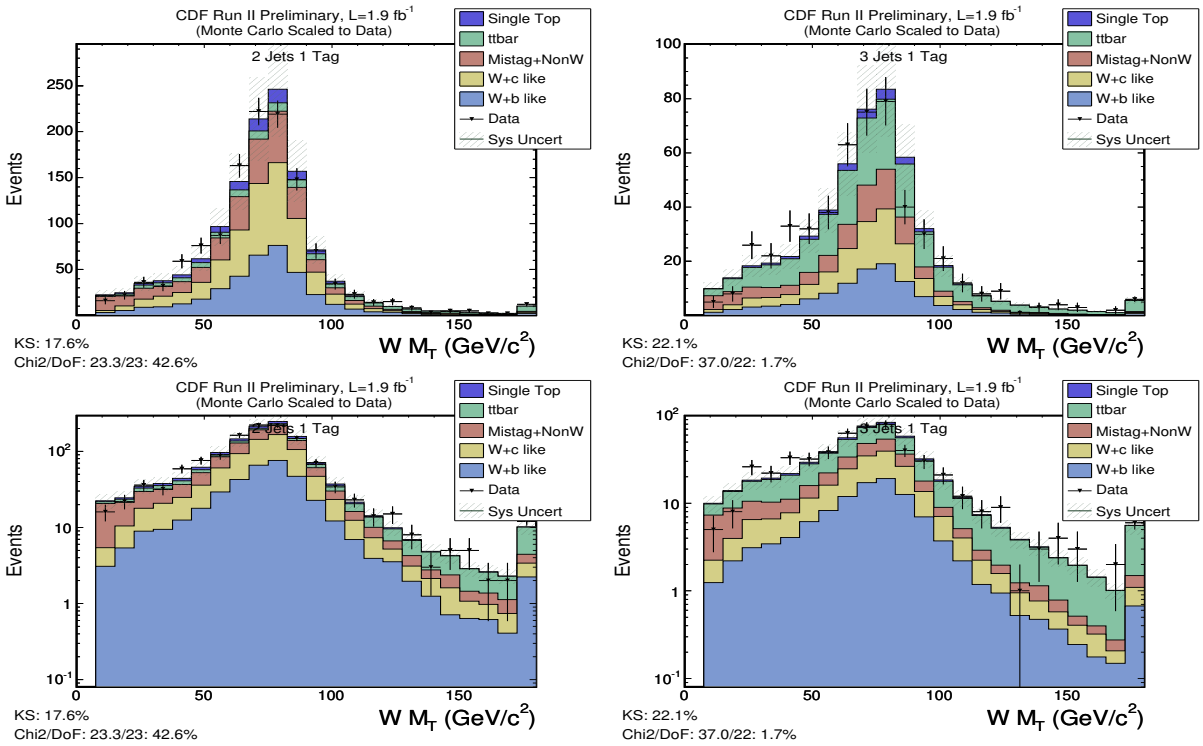

FIG. 16: Comparison of the transverse W mass model to the data for the 2 jets 1 tag channel (left) and the 3 jets 1 tag channel (right). The bottom row shows the plots on a log scale.